Renewable Energy 138 (2019) 764–774

Contents lists available at ScienceDirect

Renewable Energy

journal homepage: www.elsevier.com/locate/renene

Exploring wind farms with alternating two- and three-bladed wind turbines

Imran Hayat [a], [b], Tanmoy Chatterjee [c], Huiwen Liu [d], Yulia T. Peet [c], Leonardo P. Chamorro [e], [a], [f], *

[a] Aerospace Engineering, University of Illinois, Urbana, IL, 61801, USA
[b] Aeronautics and Astronautics, Institute of Space Technology, Islamabad, 44000, Pakistan
[c] School for Engineering of Matter, Transport and Energy (SEMTE), Arizona State University, Tempe, AZ, 85287, USA
[d] College of Water Conservancy and Hydropower Engineering, Hohai University, Nanjing, 210024, China
[e] Mechanical Science and Engineering, University of Illinois, Urbana, IL, 61801, USA
[f] Civil and Environmental Engineering, University of Illinois, Urbana, IL, 61801, USA

ARTICLE INFO

Article history:
Received 24 May 2018
Received in revised form
29 January 2019
Accepted 31 January 2019
Available online 5 February 2019

Keywords:
Two-bladed turbines
Turbine wake
Wind farms

ABSTRACT

Laboratory experiments and numerical simulations were carried out to explore potential advantages of using alternating rows of 3-bladed and 2-bladed turbines within wind farms. The power output and turbulence around the units were compared with baseline wind farms composed of 3-bladed turbines. The experimental setups consisted of two arrays of aligned turbines with streamwise separation of five and ten rotor diameters d, sharing a spanwise spacing of 2.5d. Complementary Large Eddy Simulations at full-scale Reynolds number of $Re \approx 10^9$ based on d were performed for the 5d setups. Results showed enhanced mean velocity and reduced turbulence levels in the heterogeneous wind farm as compared with the baseline in the 5d layout, which may imply lower dynamic loading; however, this was not reflected in the power fluctuation intensity. A marginal increase in the power of the 3-bladed turbines was offset by the diminished performance of the 2-bladed turbines. For the 10d cases, the benefits associated with the heterogeneous farm were negligible due to longer recovery distances. The performance of the heterogeneous wind farm did not improve over the baseline case; however, it may offer potentially lower costs of manufacturing and transportation, among others.

1. Introduction

Numerous countries have set goals for significant contribution from wind energy to their electricity supply in the medium-term future [1–3]. A recent roadmap developed for 139 countries by Jacobson et al. [4] envisions that onshore and offshore wind power will contribute to about 30% of the total energy mix by 2030, provided that 80% of the total energy conversion is from renewable energy sources. In the case of onshore installations, optimized arrangements are essential due to the large areas required to deploy the units.

Wind farm optimization has been approached from various angles, owing to its multidisciplinary nature. Particular efforts have been placed on the development of algorithms for optimizing spacing and layout [5–7]. Feng and Shen [8] developed a novel random-search algorithm based on a continuous formulation, which showed better performance than genetic algorithms. Chowdhury et al. [9] carried out a comprehensive study involving various parameters including layout, rotor diameter, number of turbines, and land area and performed a cost analysis per Kilowatt. They showed that the use of non-identical wind turbines may substantially improve the wind-farm power output. Yang et al. [10] investigated numerically the effects of the streamwise and spanwise spacing, and found the former to be more effective in improving power efficiency of turbines. Using Large Eddy Simulations (LES), Meyers and Meneveau [11] proposed an optimum turbine spacing with respect to the land area and turbine costs, and found it to be significantly larger than conventionally used spacing. Laboratory experiments by Chamorro et al. [12] showed that staggering wind turbines may lead to power increases on the order of 10% with respect to aligned counterparts. Wind turbine size

---

* Corresponding author. Mechanical Science and Engineering, University of Illinois, Urbana, IL, 61801, USA.
E-mail address: lpchamo@illinois.edu (L.P. Chamorro).

https://doi.org/10.1016/j.renene.2019.01.123
0960-1481/© 2019 Elsevier Ltd. All rights reserved.

heterogeneity has also been considered for power enhancement [13,14]. Feng and Shen [15] investigated the possibility of using multiple types of turbines in an offshore wind farm to minimize the cost of energy.

Another effective, yet less frequently used approach to enhance wind-farm power is to use different operational points in the turbines. Adaramola & Krogstad [16] studied the performance of downwind turbines as a function of the yaw angle and tip-speed ratio of upwind turbines, and the associated wind-farm efficiency. They showed that by operating the upwind turbines at non-optimal tip-speed ratio and non-zero yaw angle, the combined power increased. They demonstrated that the same technique can be used to reduce wind-turbine spacing, while achieving comparable wind-farm efficiency. This was consistent with a study by Corten et al. [17], who concluded that by operating the upwind turbines below the optimum power coefficient, not only the net wind farm power increased but the overall axial loading on turbines also decreased. Our study follows the aforementioned line of approach for wind-farm power enhancement by introducing alternating rows of 2-bladed turbines between 3-bladed turbine rows. In addition to the effect on the wake, the 2-bladed turbines have been shown to have lower energy costs than the 3-bladed turbines when operating at higher tip-speed ratios [18]. Furthermore, feasibility of operation of 2-bladed turbines at higher tip speeds allows for a reduction in the torque for a given power; this would, in turn, permit the use of lighter and thus more economical torque-sensitive components in the drivetrain [19]. These factors may contribute to further enhance power output and economic viability of a heterogeneous wind farm composed of 2-bladed and 3-bladed turbines. However, there are engineering challenges related to 2-bladed turbines that have restricted their development and adoption in the industry at the same level as their 3-bladed counterparts. The most critical challenges include higher levels of noise associated with the operation at higher tip speeds, and higher fatigue loads on the drive-train [20]. The former is not critical for offshore wind farms, whereas the latter has been mitigated in many designs with a teeter hinge similar to that used in helicopters [20].

Previous studies on 2-bladed wind turbines have primarily focused on the performance and wake characteristics of single units [21,22] and those within arrays of 2-bladed turbines [23]. Muhle et al. [21] compared the wake of 2- and 3-bladed turbines sharing the same solidity and the blade aspect ratio, all operating at maximum power coefficient, C_P. Minor differences in the mean velocity were observed especially in the far wake, but the turbulence intensity was found to be higher for the 2-bladed rotors. A faster flow recovery in the wake of the 2-bladed turbines was also reported. Newman [23] carried out a comparative PIV analysis between arrays of 2- and 3-bladed turbines with aligned configurations operating at identical C_P. They suggested that better momentum recovery downwind the 2-bladed turbines may only be effective by increasing the power output of the first few rows of an array. Despite the efforts on characterizing the power and flow around 2-bladed wind turbines, the potential benefits associated to alternating 2- with 3-bladed turbines have not been explored. This fundamental experimental and numerical study aims to contribute in that direction, where the experiments and simulations were replicated for both configurations at similar flow conditions. This study attempts to provide a better insight into the power of turbines operating within heterogeneous wind farms, and to explore unique flow features within the turbine arrays. The findings of this investigation may also allow for a more robust incorporation of the number of blades as an input parameter in various optimization techniques. The experimental and numerical setups are described in Section 2; the results and discussion are given in Section 3, and concluding remarks are provided in Section 4.

2. Setup

The experimental setup and details of the numerical simulations are described in the following subsections.

2.1. Laboratory experiments

The experiments were performed in the Eiffel-type, boundary-layer wind tunnel at the Renewable Energy and Turbulent Environment group of the University of Illinois at Urbana-Champaign. The facility has a test section of approximately 6.1 m long, 0.91 m wide and 0.45 m high. The adjustable ceiling allowed for the pressure gradient along the test section to be nearly zero during the experiments. Details of the wind tunnel can be found in Adrian et al. [24].

Miniature wind turbines with 2 and 3 blades were fabricated at the University of Illinois Rapid-Prototyping Lab using an Objet Eden 350 machine and were made of PolyJet Vero material. The geometry of the 3-bladed rotors is based on a reference model turbine from Sandia National Laboratory [25,26]. Similarly, the 2-bladed rotor was derived from the same reference model. Therefore, the solidity of the 2-bladed rotors is lower than that of the 3-bladed counterpart, whereas the aspect ratio and all other blade characteristics are the same. The model turbines share the rotor diameter $d = 120$ mm, the nacelle length $d_n = 10$ mm and the hub height $z_{hub} = 125$ mm. A Precision Microdrive 112-001 Micro Core 12 mm DC motor was used as the loading system (generator), which provided a rated power of $P_0 \approx 1$ W; additional details on the model turbine can be found in Tobin et al. [27].

The turbines were distributed in two sets. The first one (henceforth heterogeneous and denoted with the subindex $()_{3-2}$) had alternating rows of 3- and 2-bladed turbines, with the 3-bladed units in the leading row (see Fig. 1a); whereas the other set (henceforth baseline case and denoted with the subindex $()_B$), was composed of only 3-bladed turbines (see Fig. 1b). Each set included two wind-farm layouts consisting of aligned turbines with streamwise separations of $S_x = \Delta x/d = 5$ and 10 between consecutive rows, with a spanwise separation of $S_y = \Delta y/d = 2.5$. This resulted in two arrays of 7 × 3 and 4 × 3 turbines for each case. An additional dummy row was placed downwind of the last turbine row to avoid edge effects. The four layouts were operated at an incoming hub-height velocity $U_{hub} \approx 9.3\ \mathrm{m\,s^{-1}}$ resulting in a Reynolds number of $Re = U_{hub} d/\nu \approx 7.31 \times 10^4$, and a rotor tip-speed ratio of $\lambda = \omega d/(2U_{hub}) \approx 5$, where ν is the kinematic viscosity of the air and ω is the angular velocity of the rotor. An active turbulence generator placed at the entrance of the test section was used to induce incoming turbulence with a well-developed inertial subrange that spanned two decades. Details of the turbulence generator can be found in Jin et al. [28]. The turbines were operated over a rough wall with roughness elements consisting of 5 mm high chains laid parallel to the spanwise direction every 0.2 m between consecutive chains [29]; this resulted in an incoming turbulent boundary layer with a thickness of $\delta/z_{hub} \approx 2.2$ and a friction velocity of $u_* \approx 0.55\ \mathrm{m\,s^{-1}}$. Ohya [30] and Chamorro et al. [29] used similar roughness characteristics to study stratified boundary layers and wind turbine wakes over rough surfaces. Fig. 2 shows the vertical profiles of the incoming mean velocity U/U_{hub}, and turbulence intensity $I = \sigma_u/U_{hub}$, where σ_u denotes the standard deviation of the streamwise velocity fluctuations, as well as the integral length scale Λ/Λ_{hub}.

The streamwise velocity measurements were taken using a constant temperature hotwire anemometer, which was calibrated against a pitot static probe in the freestream region of the wind tunnel under very low turbulence ($I \approx 0.1\%$). Calibrations at the

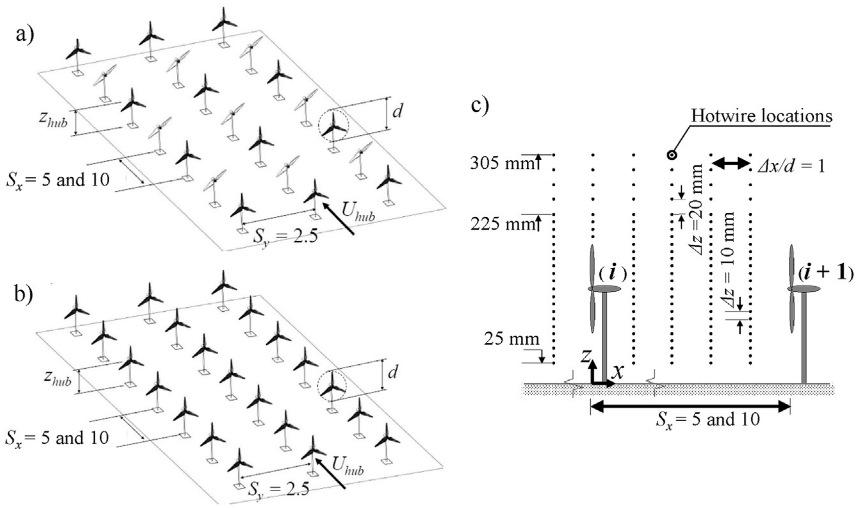

Fig. 1. a) Basic schematic of the heterogeneous wind farms with 2- and 3-bladed turbines; b) baseline case with 3-bladed turbines; c) measurement locations of the hotwire in the central plane within turbine rows i and $i+1$.

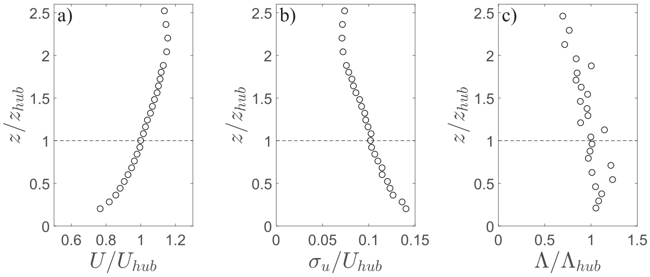

Fig. 2. Flow characteristics of the incoming turbulent boundary layer for the experiments. a) Normalized mean velocity U/U_{hub}; b) turbulence intensity σ_u/U_{hub}, and c) normalized integral length scale $\Lambda^u/\Lambda^u_{hub}$. The horizontal lines represent the normalized hub height.

beginning and the end of the experiments ensured that there was negligible voltage offset of the data acquisition system. The position of the probe was set with a Velmex traversing unit. The hotwire was positioned downwind of each turbine every $\Delta x/d = 1$. At each streamwise location, the velocity measurements were made in the central plane $y = 0$ from $z = 25$ mm ($z/z_{hub} \approx 0.21$) to $z = 225$ mm ($z/z_{hub} \approx 1.88$) every $\Delta z = 10$ mm ($z/z_{hub} \approx 0.08$) and from $z = 225$ mm to $z = 305$ mm ($z/z_{hub} \approx 2.54$) every $\Delta z = 20$ mm ($z/z_{hub} \approx 0.17$); see Fig. 1c. The hotwire readings were sampled at 10 kHz for measurement periods of 60 s using a Dantec dynamic system. A room temperature of 23±0.5°C was maintained throughout the experiments to avoid thermal drift of the voltage signal of the hotwire anemometer. The instantaneous turbine voltages were measured from the central turbine in each row, at 10 kHz for a period of 120 s using an USB-1608HS data acquisition system, where the power was calculated from the voltage and the terminal resistance (2Ω) of the generator [27].

2.2. Numerical simulations

The LES of the wind turbine arrays were carried out in the Integrative Simulations and Computational Fluids Lab at the Arizona State University, to complement the wind-tunnel experiments at a field-scale Reynolds number of $Re \approx 10^9$.

2.2.1. Numerical method

The simulations considered 7 × 3 turbine arrays with $S_x = \Delta x/d = 5$, $S_y = \Delta x/d = 2.5$ corresponding to the experimental setup described in Section 2.1. The numerical method implements a variational formulation of the Navier-Stokes (NS) equations involving Galerkin projection using open-source spectral element solver Nek5000 [31] in $\mathbb{P}_N - \mathbb{P}_{N-2}$ formulation (see Deville et al. [32] for more details). The domain is partitioned into hexahedral elements in 3D, and within each element any variable can be expanded into a series of orthogonal basis functions (Lagrange-Legendre polynomials) discretized using grid points clustered towards the element boundaries known as Gauss-Lobato-Legendre (GLL) points, which are the roots of the basis function polynomials. For smooth solutions, an exponential convergence can be achieved with an increasing order of the polynomials. The current algorithm in Nek5000 was optimized to achieve perfect scalability in parallel implementation for up to 1,000,000 processors [31].

For the simulations in neutral atmospheric conditions, the LES with near-wall modeling was implemented in Nek5000 using the wall-damped Smagorinsky-based eddy viscosity closure [33], and shear stress boundary conditions at the bottom ‘wall’ to model the near-wall logarithmic layer. Fig. 3 illustrates that the time-averaged streamwise velocity gradient $\phi(z)$ for the spectral element model [34] is close to the state-of-the-art dynamic model [35], and shows a consistent trend of a logarithmic layer, i.e., $\phi(z) \approx 1$. See Chatterjee and Peet [34] for more details regarding the model implementation and validation.

2.2.2. Actuator line model

The wind turbines are modeled using a state-of-the-art actuator line (AL) model [36]. There, the blades with the airfoil cross sections are divided into elements, similar to the Blade Element Momentum Theory (BEM). The local lift (L) and drag (D) forces experienced by each element are calculated as $(L, D) = \frac{1}{2} C_{(l,d)}(\alpha)\, \rho\, V_{rel}^2\, c\, w_d$, where c and w_d are the chord-length and the blade element width. The local angle of attack, α, is computed from the relative velocity, V_{rel}, the streamwise velocity, u ($\tilde{u}$ in LES), and the pitch angle, γ (Fig. 4). The lift $C_l(\alpha)$ and drag $C_d(\alpha)$ coefficients in this study correspond to the NACA 44xx airfoil series and are taken from wind-tunnel measurements performed on NACA airfoils at a chord $Re = 6 \times 10^6$ [37]. The local lift and drag values are used in the

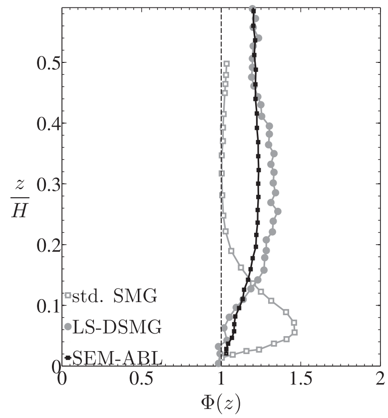

Fig. 3. Time averaged normalized streamwise velocity gradient $\Phi(z) = \kappa(z/u_*)dU/dz$ for the standard Smagorinsky (highly diffusive), the Lagrangian averaged scale-dependent dynamic Smagorinsky [35] and the current wall damped standard Smagorinsky [34] models in spectral elements for the neutral ABL precursor; $\kappa = 0.41$ is the von Karman constant, U is the mean velocity, and u_* is the friction velocity of the turbulent boundary layer.

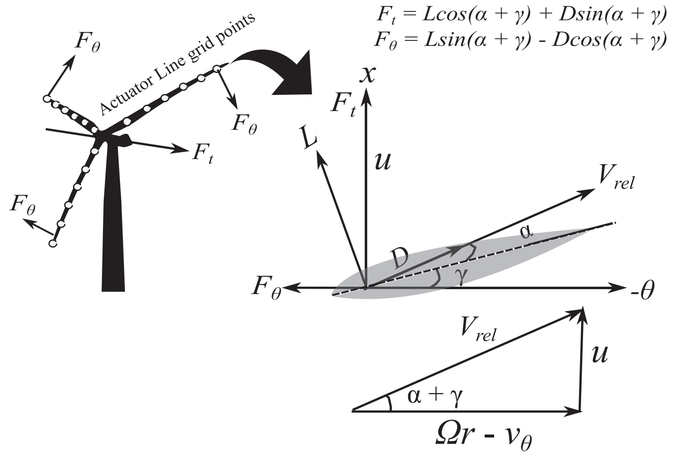

Fig. 4. Actuator line forces obtained at the nodal points of the turbine blades. V_{rel} is obtained from the velocity triangle. F_t and F_θ are the axial thrust and rotational forces on the turbine blades due to the lift (L) and drag (D) forces.

computation of the local aerodynamic force $\vec{f} = L\vec{e_L} + D\vec{e_D}$, where $\vec{e_L}$ and $\vec{e_D}$ are the unit vectors in the direction of the local lift and drag.

The reaction force experienced by the fluid from each blade element is distributed smoothly across the neighboring mesh points, and the total reaction force is a summation of the forces from all blade elements of all wind turbines, $N_{b,tot}$, given as the actuator line force in the NS equations:

$$\tilde{\mathbf{F}}_{AL}(x,\ y,\ z,\ t) = -\sum_{i=1}^{N_{b,tot}} \vec{f}(x_i,\ y_i,\ z_i,\ t)\ \eta_\varepsilon\left(\left|\vec{r} - \vec{r_i}\right|\right), \tag{1}$$

Where $\vec{r} = (x, y, z)$, $\eta_\varepsilon(d)$ is a Gaussian function in the form of $\eta_\varepsilon(d) = 1/\varepsilon^3\pi^{3/2}\exp[-(d/\varepsilon)^2]$, and $\varepsilon = 2\,w_d$ is used in the current study as suggested in Troldborg [36] and Churchfield et al. [38] for optimum results. The wind turbine power is calculated from the aerodynamic torque T experienced by each turbine as:

$$P = T \times \Omega, \tag{2}$$

where Ω is the rotational speed of the rotor. The torque is computed from the azimuthal forces F_θ calculated on the blade elements (see Fig. 4) as $T = \sum_{i=1}^{N_{b,turb}} r_i F_{\theta\ i}\,\Delta r_i$, where $N_{b,turb}$ is the number of blade elements corresponding to a particular turbine. The AL model is more advanced than the actuator-disk model [39,40] commonly used in numerical computations of large wind farms, in its capability to capture the tip vortices being shed in the near-wake [36,41].

2.2.3. Numerical setup

All wind-farm layouts are driven by a concurrent neutral ABL precursor simulation (See also [42,43]). The time-dependent inflow conditions (with the inflow boundary located 2.5d upwind of the first row of turbines) are obtained from a synchronously-computed turbulent flow solution at the midplane location of the ABL domain ($x/d = 10\pi$), which is spectrally interpolated to a finer wind turbine array domain at each time step. A downwind development section of 30d past the last row of turbines combined with the stabilized outflow boundary condition [44] are used to prevent numerical instabilities associated with the exiting of strongly-vortical wake flows. Table 1 documents the size of the domain, the number of elements, and the total number of grid points used for the simulations of the wind turbine arrays and the neutral ABL. For an adequate resolution of wake-blade interactions in the rotor region and the tip vortices shed by the turbines, the suggested number of blade elements per rotor radius is approximately 30 [36,38], which was used in the current study. The background LES grid in the wind-turbine layouts was accordingly refined to a resolution of $\approx 0.02d$ in the rotor region in all three directions, while featuring grid sizes of $\approx 0.2d$ far away from the rotors, similar to the methodology described in Chatterjee and Peet [45]. Neutral ABL grid does not need a local refinement and thus contains less elements and grid points.

The simulations considered the same non-dimensional hub-height, $z_{hub}/d = 1.04$, and $\lambda \approx 5$ of the experiments (§ 2.1). Note that $y = 0$ in the LES corresponds to the central plane containing the middle column of the turbines similar to the experiments. The domain had a vertical span coincident with the boundary layer thickness $\delta/d = 10$, and considered symmetric boundary conditions at the top. This resulted in a blockage ratio (ratio of the frontal area of the turbine rotors in the spanwise cross-section to the cross-sectional area of the domain) of less than 3.2%. The aerodynamic roughness length ratio $z_0/\delta \approx 4 \times 10^{-3}$ is similar to the experiments. The spanwise extent of the domain was 7.5d, given the number of turbines and their spanwise separation that matched the experiments, and enforced periodic boundary conditions. The width of the domain, 0.75δ, was sufficient to sustain the turbulence at $Re \approx 10^9$, in line with the analysis of Jimenez and Moin [46]. They showed that domains wider than 0.5δ would be sufficient to sustain the turbulence at $Re > 5,000$. This is further corroborated in Fig. 5, which shows a snapshot of the instantaneous velocity field at the

Table 1
LES cases for the baseline and heterogeneous configurations, as well as the neutral ABL precursor. N_i^e is the number of spectral elements in the i^{th} direction, N_{xyz} is the total number of grid points used in the computational domain, d is the rotor diameter, and the hub-height $z_{hub} = 1.04d$. Similar quantities for a neutral ABL simulation [34] is provided for comparison.

Case	Geometry	$N_x^e \times N_y^e \times N_z^e$	N_{xyz}
Baseline	$20\pi d \times 7.5d \times 10d$	$48 \times 32 \times 24$	1.22×10^7
Heterogeneous	$20\pi d \times 7.5d \times 10d$	$48 \times 32 \times 24$	1.22×10^7
Neutral ABL	$20\pi d \times 10\pi d \times 10d$	$30 \times 20 \times 24$	5.02×10^6

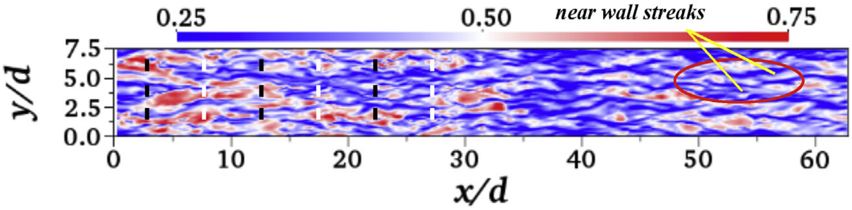

Fig. 5. Snapshot of the instantaneous streamwise velocity at $z/d = 0.25$ showing the persistence of turbulent velocity streaks (baseline configuration from the LES data). The white turbines represent the 3-bladed rotors that are in place of the 2-bladed units in the heterogeneous configuration; whereas black turbines represent the 3-bladed rotors, which did not change between the heterogeneous and baseline cases.

vertical location $z/d = 0.25$; there, multiple streaky structures characteristic of the boundary layer turbulence are visible. The cut-off of the spectral scales larger than the domain size (here $7.5d$ in the spanwise spectrum) was previously shown not to influence the dynamics of the smaller scales that are resolved [14,47,48], whereas the resolved scales in the current simulations are in the range that dominate the wind-turbine power production [45,49,50]

The LES included wind farms corresponding to the baseline and heterogeneous layouts with $S_x = 5$. After the statistical stationarity is achieved in each simulation, snapshots are collected every 10^{-4} flow-through time (every timestep) for a timespan of 80 flow-through times for acquiring turbulent statistics. The flow-through time is defined as $T_e = 20\pi d/U_{bulk}$, where U_{bulk} is the incoming bulk mean velocity.

The incoming turbulent flow characteristics resulting from the LES of the neutral ABL, namely the mean velocity, the turbulence intensity and the integral length scale are shown in Fig. 6. These statistics are on the order of those obtained in the current wind-tunnel experiments. The LES have been carried out on the Stampede supercomputer of the Texas Advanced Computing Center. The details of the computational cost for performing the simulations, including the number of processors, the total number of time steps and the total computational time in CPU hours for each of the simulations, are presented in Table 2.

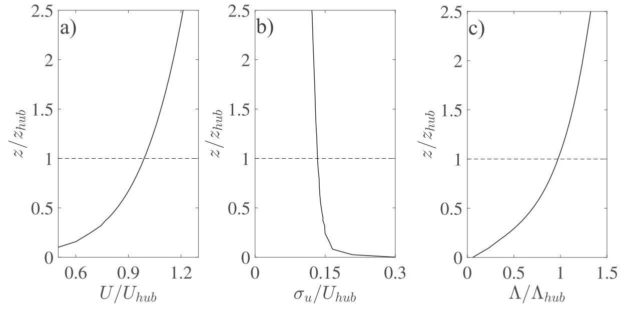

Fig. 6. Flow characteristics of the incoming turbulent boundary layer for the LES. a) Normalized mean velocity U/U_{hub}, b) turbulence intensity σ_u/U_{hub}, and c) normalized integral length scale $\Lambda^u/\Lambda^u_{hub}$. The horizontal lines represent the normalized hub height.

3. Results and discussion

In this section, we inspect the distinctive flow features and power from the heterogeneous wind farms and discuss potential benefits over the baseline cases. The differences in the flow are described via the mean flow statistics, and the spectral decomposition of the flow; whereas the differences in performance characteristics are assessed with the distinctive changes in the turbine power. For the sake of brevity, the results most relevant to the goal of this study are presented using either one of the two spacing scenarios unless there is a difference worth highlighting.

The experimental results involving the statistics and the turbine power are further complemented using LES data. As shown later, the similarity of the results obtained with the wind-tunnel experiments at $Re \sim O(10^5)$ and with the LES at $Re \sim O(10^9)$ gives confidence in the subsequent analysis of the flow physics and the resulting power performance of the heterogeneous and baseline layouts.

3.1. Mean flow and turbulence statistics

Basic assessment of the changes induced with the 2-bladed turbines is first illustrated with the differences of the streamwise velocity component between the heterogeneous (U_{3-2}) and the baseline cases (U_B) in the central plane $y = 0$; i.e., $\Delta U(x,z)/U_{hub} = (U_{3-2} - U_B)/U_{hub}$. As shown in Fig. 7 for the experimental cases with $S_x = 5$ and 10, $\Delta U(x,z)/U_{hub}$ is particularly prominent in the near wake. Note that for $S_x = 5$ substantial velocity differences extend up to the subsequent turbine in the wake of 2-bladed turbines, where $\Delta U/U_{hub}$ at the hub-height of subsequent turbine is higher than that at the same position in the wake of 3-bladed turbines. Spanwise (rotor) averaged values of $\Delta U/U_{hub}$ along the hub-height (not shown here) of the subsequent turbine revealed that this quantity is higher than 0.05 in the wake of the 2-bladed turbines, whereas it is lower than 0.02 in the wake of the 3-bladed turbines. However, $\Delta U/U_{hub}$ is mostly confined in the very near wake in the case with $S_x = 10$. In this case, larger spacing allows for better interaction between the wakes and the outer flow. This suggests that potential benefits associated with the 2-bladed rotors appears to be within relatively short turbine spacing.

Similarly, the differences on the turbulence intensity between the two configurations $\Delta I = -sgn(\sigma^2_{3-2} - \sigma^2_B)\left|\sigma^2_{3-2} - \sigma^2_B\right|^{1/2}/U_{hub}$ in

Table 2
Computational cost of the LES Simulations. Neutral ABL precursor simulations have been run currently with the wind turbine simulations in each configuration, the allocation of 2048 processors among the precursor and wind turbine domains has been done in proportion to their corresponding grid sizes. N_{steps} – total number of timesteps in the simulations. Δt – size of the timestep used in the simulations.

Case	Processors	Time/Timestep	Δt	N_{steps}	CPU-hours
Baseline + precursor	2048	2.75E-01	$10^{-4}T_e$	12×10^5	330,000
Heterogeneous + precursor	2048	2.75E-01	$10^{-4}T_e$	12×10^5	330,000

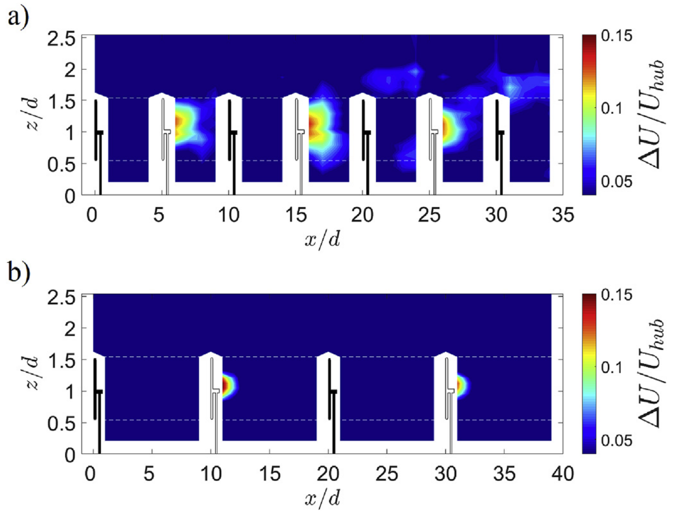

Fig. 7. Distribution of the mean streamwise velocity difference $\Delta U/U_{hub} = (U_{3-2} - U_B)/U_{hub}$ between the heterogeneous and baseline cases in the vertical plane $y = 0$ for the a) $S_x = 5$, and b) $S_x = 10$ layouts obtained from the experimental data. The horizontal dashed lines represent top and bottom tip heights. White turbines represent those with the 2-bladed rotors.

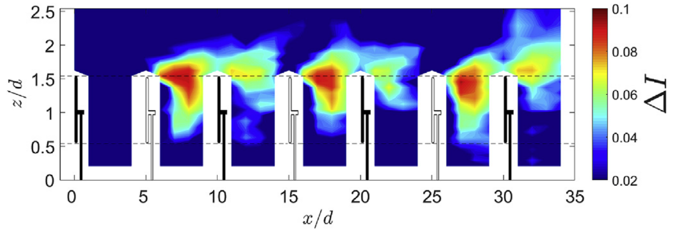

Fig. 8. Distribution of the turbulence intensity difference $\Delta I = -sgn(\sigma^2_{3-2} - \sigma^2_B)\left|\sigma^2_{3-2} - \sigma^2_B\right|^{1/2}/U_{hub}$ between the heterogeneous and baseline cases in the vertical plane $y = 0$ for the $S_x = 5$ layout obtained from the experiments. White turbines represent those with the 2-bladed rotors.

the experiments are shown in Fig. 8. Here, σ denotes the standard deviation of the velocity fluctuations. The case for $S_x = 5$ is shown in Fig. 8; the other case did not show major differences, and is not shown for brevity. The figure reveals a non-negligible reduction in the turbulence levels of the flow impinging the turbines immediately downwind of the 2-bladed units; this effect persists beyond the adjacent rows into the wake of the downwind row. The overall lower turbulence intensity of the heterogeneous wind farm is expected to result in a lower flow-induced turbulent loading on the turbines (not taking into account the differences in the dynamic characteristics of the rotors due to the differences in the inertia).

The LES results for the $\Delta U/U_{hub}$ and ΔI are presented in Fig. 9 for $S_x = 5$. Similar to the experiments, $\Delta U/U_{hub}$ exhibited higher values in the rotor region downwind of the 2-bladed turbines indicating the higher velocities and weaker wake effects behind these turbines. The turbulence intensity is also lower downwind of the 2-bladed turbines, consistent with the experiments. Some differences are observed between the simulations and experiments in the induced turbulence in the wake of the 2-bladed turbines above the top tip. Additionally, ΔI for the first (3-bladed) row of turbines between the heterogeneous and baseline configurations in the LES are noticeable. These differences are likely caused by the interaction of the upwind flow with the downwind turbine rows. Indeed, a wind farm causes a 'blockage' effect to the incoming stream [51,52] that alters the flow patterns right upwind. A supplied turbulent inflow solution obtained from a precursor ABL without wind turbines in the simulations interacts with this blockage differently for different wind-farm configurations. This results in slightly different turbulence intensity between the cases even in the first row of turbines (with the same rotor), while the flow velocities for the first row are the same in both configurations. While this phenomenon might have some effect on the overall 'wake' of lower turbulence intensity in the heterogeneous case above the turbines, the strong reduction of turbulence intensity behind the 2-bladed turbines as compared to the 3-bladed turbines is consistent with experiments. Also, noticeable from the numerical and experimental ΔI distribution, and from the velocity deficit, is the streamwise growth of the region where the differences are pronounced. This observed growth is a manifestation of the differences of the internal layer [53] growth between the heterogeneous and baseline layouts. These results are also understandable when inspecting Figs. 10 and 11, where a quicker velocity recovery downwind of the 2-bladed turbine rows and a slower growth of the internal layer are evident. Inspection of the instantaneous velocity magnitude snapshots shown in Fig. 12 for the heterogeneous and the baseline layouts allows us to compare the large-scale turbulence motions induced by the turbine arrays in both cases. It is interesting to note that both cases depict similar features of the large-scale downdrafts from a high-speed velocity region associated with the counter-rotating roller modes observed in VelHulst and Meneaveau [40] as well as in Peet and Chatterjee [54]. This illustrates that the large-scale dynamics is essentially similar in both cases, and the downdraft mechanism [39] still plays an important role in the power generation, in addition to a streamwise interception of the turbulence by the turbine rotors.

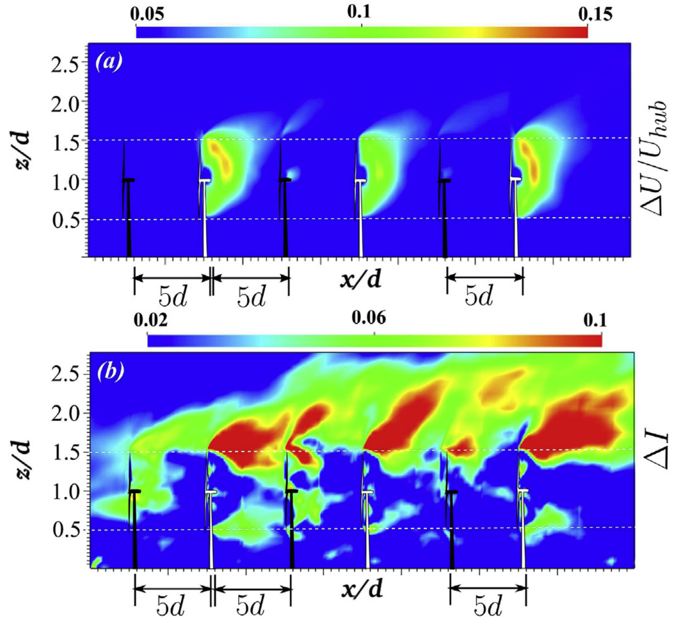

Fig. 9. Distribution of the a) mean streamwise velocity difference $\Delta U/U_{hub} = (U_{3-2} - U_B)/U_{hub}$, and b) turbulence intensity difference $\Delta I = -sgn(\sigma^2_{3-2} - \sigma^2_B)\left|\sigma^2_{3-2} - \sigma^2_B\right|^{1/2}/U_{hub}$ between the heterogeneous and baseline cases in the vertical plane at $y = 0$ for the $S_x = 5$ layout from the LES data. The horizontal dashed lines indicate the top and bottom tip heights. White turbines represent those with the 2-bladed rotors.

3.2. Velocity spectra

The compensated spectral difference of the streamwise velocity

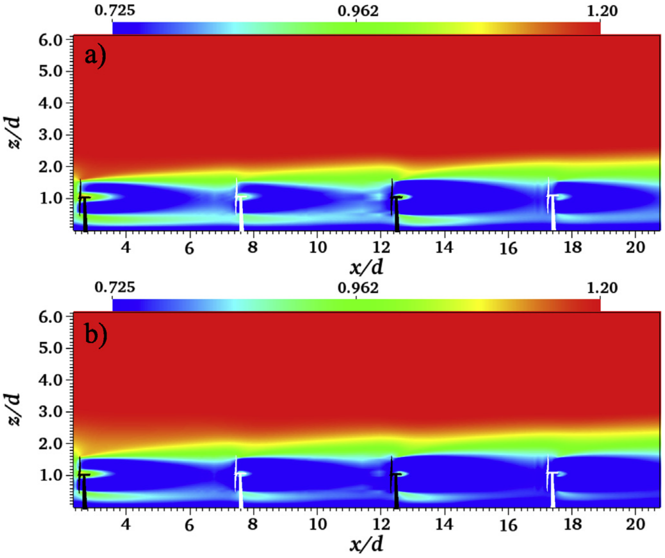

Fig. 10. Time-averaged streamwise velocity U/U_{hub} at the central plane, $y = 0$, for the first four rows of turbines from the LES data. a) Heterogeneous configuration, b) baseline. Contours zoomed to 60% of the domain height. White turbines represent those with the 2-bladed rotors.

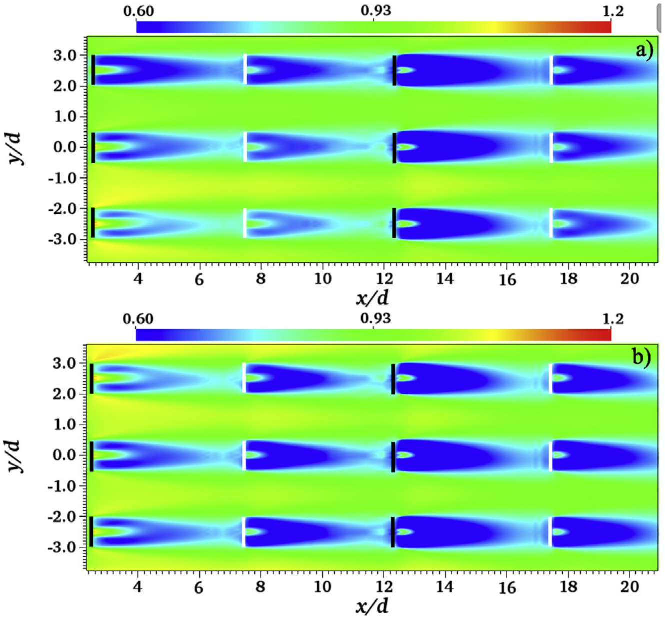

Fig. 11. Time-averaged streamwise velocity U/U_{hub} at the hub-height, $z/d = 1.04$, zoomed in for the first four rows of turbines from the LES data. a) Heterogeneous configuration, b) baseline. White turbines represent those with the 2-bladed rotors.

$\Delta(f\Phi_u)/u_*^2 = (f\Phi_B - f\Phi_{3-2})/u_*^2$, where f is the frequency and Φ is the velocity spectrum, between the baseline case and the heterogeneous wind farms was calculated to assess the redistribution and generation of coherent motions. Those along the central plane of the wind farms ($y = 0$) at the top tip height and at the hub-height are shown in Fig. 13 for the $S_x = 5$ experimental cases. Noticeable differences resulted within a frequency band $fd/U_{hub} \in [10^{-1}, 10^0]$; these motions are in the range of those able to modulate the structure of instantaneous power of the turbines [50]. As noted in the wake, the 2-bladed turbines clearly dampened the motions in that range, which partially extended through the downwind row.

Consistent with the distribution of ΔI (Fig. 8), relatively minor differences in the compensated spectra extended to the hub height, which were contained within a similar range of scales ($fd/U_{hub} \in [10^{-1}, 10^0]$). Note that such effect did not extend to the downwind row. At the bottom tip height (not shown here), the compensated spectral difference between the two configurations resulted practically negligible, which is likely due to strong modulation of the wall. Complementary insight is obtained with the compensated velocity spectrum at the hub height in the heterogeneous wind farm shown in Fig. 14. The dominant frequency range was contained within $fd/U_{hub} \in [10^{-1}, 10^0]$, as reported by Jin et al. [28] and also observed in experiments by Chamorro et al. [55]. In this range, the spectral energy contribution of the 2-bladed rotors was clearly lower than the 3-bladed turbines. This illustrates the effect of the number of blades in filtering the flow.

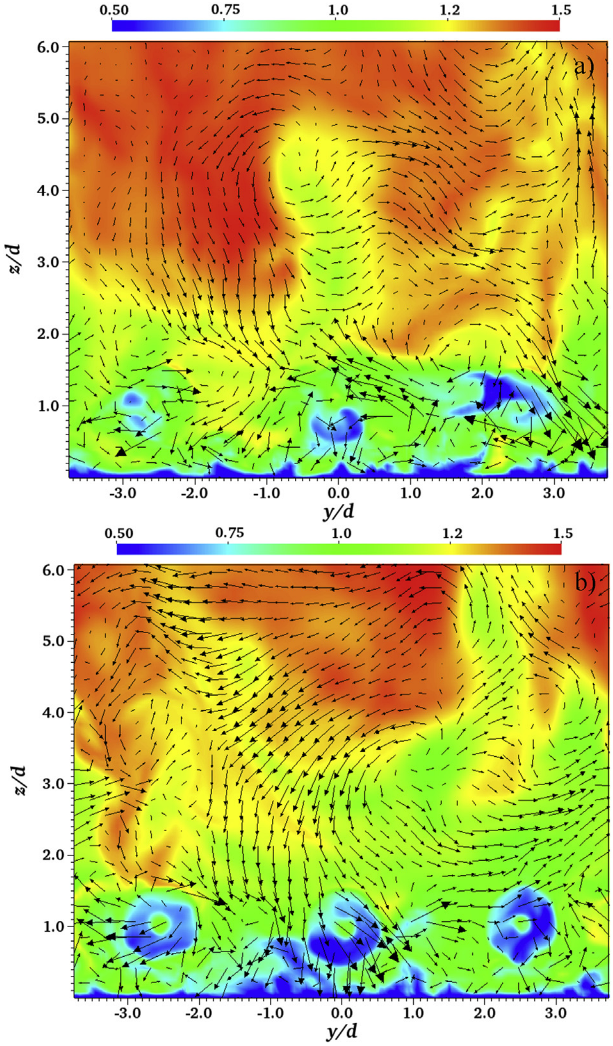

Fig. 12. Instantaneous snapshots of velocity magnitude contours $\sqrt{u^2 + v^2 + w^2}/U_{hub}$, with in-plane velocity vectors (v, w) for the second row of the turbines from the LES data. a) Heterogeneous configuration (second row corresponds to the 2-bladed turbines), b) baseline.

Fig. 15a illustrates profiles of the compensated spectra ($f\Phi_u$) at the top-tip height for the heterogeneous and baseline cases. The spectral peaks varied with the configuration and distance from the first row. The relatively larger spacing between consecutive helical vortices in the case of the 2-bladed turbines resulted in weaker interactions between the tip vortices in the near wake, which are associated with the onset of large-scale vortex shedding [56]. The

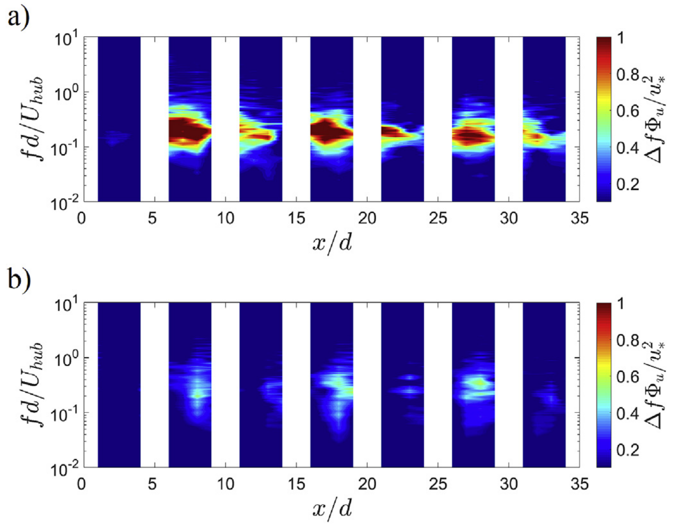

Fig. 13. Contours of the compensated spectral difference of the streamwise velocity component $\Delta(f\Phi_u)$ between the heterogeneous wind farm and baseline cases at the center plane for the $S_x = 5$ experimental layout. a) Top tip height, b) hub height.

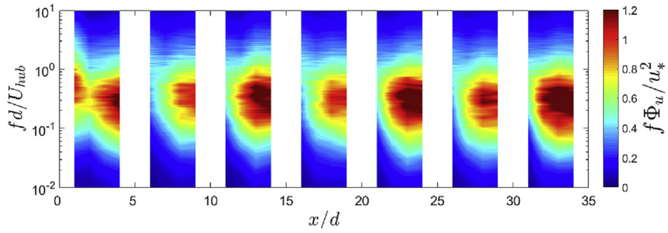

Fig. 14. Compensated velocity spectrum $(f\Phi_u)$ from the experiments at the hub height in the $S_x = 5$ heterogeneous wind farm along the central plane.

lower solidity of the 2-bladed rotors should result in lower strength of the shed vortices, similar to what was observed for high-porosity discs by Medici and Alfredsson [57]. This may be responsible for relatively larger power fluctuations and fatigue loads on the 3-bladed units. The particular case at $x/d = 16$ (or one rotor diameter downwind of the 3rd row) is shown in Fig. 15b. The peak of the compensated spectrum is observed to be at normalized frequency of $fd/U_{hub} \approx 0.2$, or $St = fd/U_{hub,local} \approx 0.26$, where $U_{hub,local}$ is the incoming velocity at hub-height seen by the local turbine.

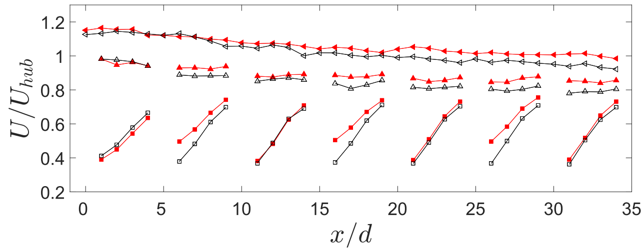

Fig. 16. Streamwise velocity distribution U/U_{hub} from the experiments obtained in the central plane of the $S_x = 5$ layouts. Red and black lines denote the heterogeneous and baseline cases. $\square - (z - z_{hub})/d = 0$, $\triangle - (z - z_{hub})/d = 0.5$, $\triangleleft - (z - z_{hub})/d = 0.83$. (For interpretation of the references to colour in this figure legend, the reader is referred to the Web version of this article.)

Finally, it is worth describing the mean flow recovery as a first measure of power output of the wind farms. Fig. 16 illustrates the distribution of the mean streamwise velocity component at the hub and top-tip heights as well as at a height above the wind farm for the $S_x = 5$ layouts. At hub-height, the baseline case exhibited higher flow rate recovery, which is likely attributed to the higher turbulent interaction of the wake and outer flow, as seen in Fig. 13. However, higher velocity occurred in the heterogeneous wind farm, which is more important for the overall power output of the wind farm. The experimental results complemented by the LES data in Fig. 17 depicted similar behavior. Both the hub-height region and above it show higher velocities in the heterogeneous layout compared to the base case. Note that distinctive mixing induced different velocity distributions above the farm (Fig. 16). There, the baseline exhibited larger velocity deficit, suggesting a larger wake expansion in the baseline. This is consistent with the growth of the internal layer shown in Fig. 10. Similar observations were made regarding the differences in the rate of recovery and wake expansion of 2- and 3-bladed turbines by Medici [22].

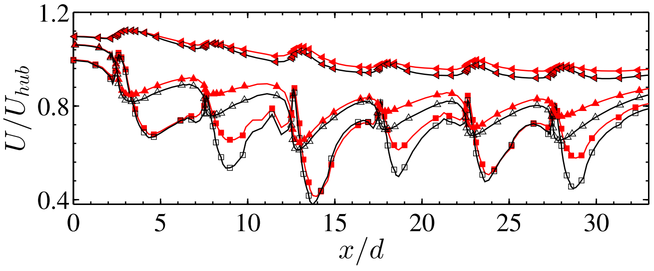

Fig. 17. Streamwise velocity distribution U/U_{hub} from the LES obtained in the central plane of the $S_x = 5$ layouts. Red and black lines denote the heterogeneous and baseline cases. $\square - (z - z_{hub})/d = 0$, $\triangle - (z - z_{hub})/d = 0.5$, $\triangleleft - (z - z_{hub})/d = 0.83$. (For interpretation of the references to colour in this figure legend, the reader is referred to the Web version of this article.)

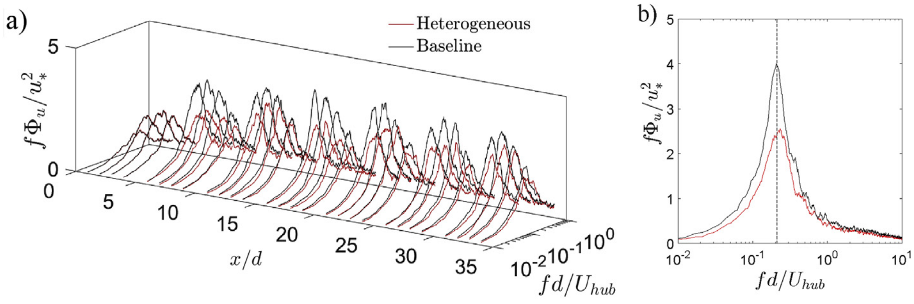

Fig. 15. a) Compensated spectra $f\Phi_u/u_*^2$ for the heterogeneous wind farm and baseline cases obtained from the experimental data; b) same as a) at $x/d = 16$. The vertical dashed line corresponds to the peak frequency at $fd/U_{hub} \approx 0.2$.

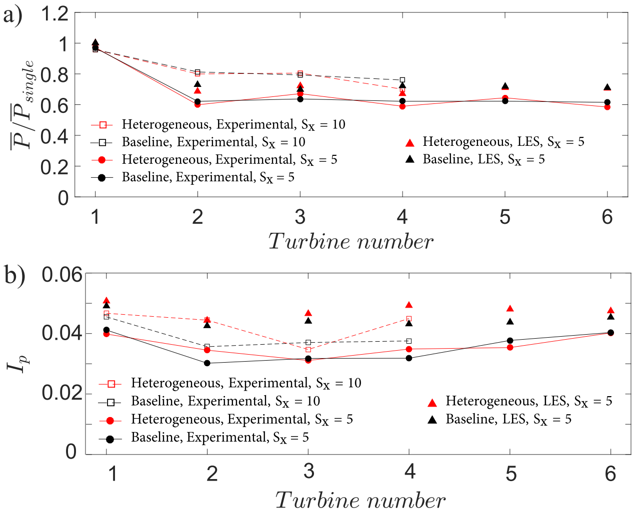

Fig. 18. a) Mean power of turbines normalized by that of a single turbine with the same number of blades operating in the background boundary layer turbulent flow $\overline{P}/\overline{P}_{single}$; b) power fluctuation intensity, $I_p = \sigma_p/\overline{P}$.

3.3. Power output

Fig. 18 shows the normalized mean power $\overline{P}/\overline{P}_{single}$ and power fluctuation intensity $I_P = \sigma_P/\overline{P}$ in the turbines from experiments and LES. Here, σ_P denotes the standard deviations of the power fluctuations and $\overline{P}_{single} \approx 0.43$ W and 0.58 W for the 3- and 2-bladed turbines (experiments). The bulk power was roughly reached past the 2nd row in the $S_x = 5$ cases. Note that in the heterogeneous wind farm, the 3-bladed turbines appear to perform slightly better than their counterparts in the baseline case due to the higher momentum available in the wake of the 2-bladed rotors (Fig. 16). Consistent with the observations made in section 3.1, there are minor differences between the two configurations with respect to mean power performance for the first three rows in the $S_x = 10$ layout.

In general, the intensity of the power fluctuations decreased after the first row, as the large-scale structures in the incoming flow lose coherence. Past the first row, I_P showed a gradual increase for the $S_x = 5$ layout, possibly due to better mixing of wake with the outer flow at downwind locations, whereas equilibrium appeared to be attained from the second row in the $S_x = 10$ layout. The LES data for the $S_x = 5$ layout showed similar trends. The fluctuations of 2-bladed turbines were in general greater than the 3-bladed turbines. In particular, this difference was significantly larger for the $S_x = 10$, possibly due to the pronounced effect of a load imbalance for the 2-bladed rotors at higher velocities and their lower inertia, which made them more susceptible to turbulent loading. However, from the experimental results, the 3-bladed turbines immediately downwind of 2-bladed ones showed lower fluctuation intensity than their counterparts in the baseline case, consistent with a reduction of turbulence intensity in the wake of the 2-bladed turbines. The differences in intensity appeared minor deep inside the farm (row 6). Note that this effect was absent in the LES results, where the turbulence intensity difference between the two configurations occurred mainly above the top tips. The overall power fluctuation intensity of the wind farm $I_{p,wf}$ is presented in Table 3, which was calculated from equation (3) [58] using the experimental and the LES data. It takes into account the non-negligible covariance of the turbine pairs. The competing effects of the two rotors, namely the higher I_p of the 2-bladed turbines and the lower I_p of the 3-bladed counterparts operating in the wake of the 2-bladed turbines, resulted in $I_{p,wf}$ for the heterogeneous wind farm comparable to that of the baseline. The higher $I_{p,wf}$ for the $S_x = 10$ layout from the experimental data is consistent with the better entrainment of the large energetic motions from the outer flow into the wake. The LES data for the $S_x = 5$ shows a consistent trend with the experiments; the heterogeneous wind farms exhibited a slightly higher overall intensity in the turbine power fluctuations. The fact that the LES results predict consistently higher values of both the normalized turbine power and the power fluctuation intensity may be explained by a persistence of a more energetic turbulence in the outer layer of the incoming ABL at field scale, which is also noted in Fig. 6.

Table 3
Total power fluctuation of wind farm obtained from experiments and LES.

Wind farm type	S_x	$I_{p,wf}$
Heterogeneous (exp)	5	0.032
Baseline (exp)	5	0.029
Heterogeneous (LES)	5	0.047
Baseline (LES)	5	0.044
Heterogeneous (exp)	10	0.034
Baseline (exp)	10	0.034

$$I_{p,wf} = \left[\sigma^2\left(\sum_{i=1}^{N} P_i\right)\right]^{1/2} \Bigg/ \sum_{i=1}^{N} \overline{P}_i$$
$$\sigma^2\left(\sum_{i=1}^{N} P_i\right) = \sum_{i=1}^{N} \sigma^2_{P_i} + 2\sum_{i=1}^{N}\sum_{j>i}^{N} Cov(P_i, P_j) \qquad (3)$$

To inspect the structure of the power fluctuations and the effects of the incoming turbulence structure, selected spectra of the power output (Φ_p) are illustrated together with the spectra of the incoming velocity (Φ_u) at the hub-height in Fig. 19, for the $S_x = 5$ heterogeneous wind farm. In Fig. 19a, the approach velocity to the first row exhibits higher spectral energy content in the large-scale motions as compared with that of the second row; whereas the trend is opposite for the intermediate and smaller scales. Note that for the flow approaching to the turbines in the second row, the inertial subrange resulted shorter and started at a higher frequency. The change in the flow structure had a direct influence on the structure of power fluctuations. This is consistent with previous studies by Tobin et al. [59], where the modulation of turbine power by the incoming hub-height velocity was established. They reported a tuning-free transfer function $G(f) \propto f^{-2}$ for the intermediate frequencies, which accounts for the non-linear response of the turbine power to the flow defined as $\Phi_p = G(f)\Phi_u$. The spectra of power in Fig. 19 follow this trend, with a power law decay of f^{-2} and $f^{-5/3-2}$ in a frequency range below and within inertial subrange. Corresponding to the structure of the incoming flow, the region of the power spectrum with $f^{-5/3-2}$ power law decay is shifted to higher frequencies for the second row with respect to the first row. Furthermore, the spectral content of the power of the second row was reduced at comparatively low frequency due to the dampening of the large scale motions by the first row. Comparison of the spectra between the fifth and sixth rows in Fig. 19b shows an increase in the spectral energy content of power output across all scales for the sixth row (2-bladed turbine), consistent with the slightly higher levels of energy content in the approach flow to the sixth row compared with the fifth row.

4. Conclusions

The power and wake characteristics of the heterogeneous wind

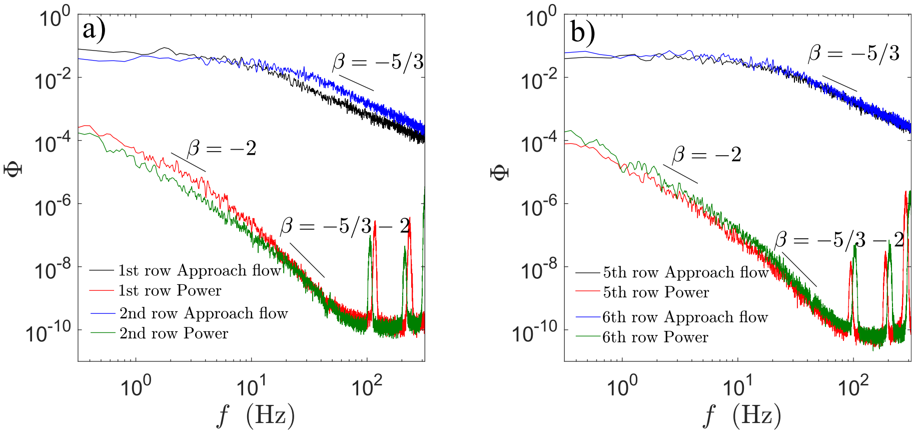

Fig. 19. Spectra of the turbine power fluctuations obtained from the experiments for the $S_x = 5$ heterogeneous wind farm. a) First and second rows, b) fifth and sixth rows. Spectra of the approach hub-height velocity at 1d upwind of each turbine are included for reference.

farms with alternating rows of 3-bladed and 2-bladed turbines were investigated and compared with those of a baseline model farm composed of all 3-bladed turbines considering two layouts. Overall, the experiments and the LES depict similar trends in the mean flow characteristics, turbulent statistics and wind turbine power. Some quantitative discrepancies that are observed between the experiments and simulations can be attributed to the differences in the Reynolds number, the incoming boundary layer characteristics, and the ratio of the hub-height to the boundary layer thickness z_{hub}/δ. Assessment of the impact of each effect deserves attention in a future work.

The heterogeneous layout with $S_x = 5$ exhibited enhanced mean velocity in the wakes and possibly lower flow-induced turbulent loadings on the downwind turbines due to lower turbulence levels. The spectral analysis shed light on the differences of the two types of rotors. Despite that the presence of 2-bladed turbines may have benefits associated to lower turbulent loading, such effects were not clearly translated in power fluctuation intensity, indicating a dominant role of the structural characteristics of the rotors in determining the power fluctuations. A marginal increase in the power output of the 3-bladed turbines operating in the higher momentum wake of the 2-bladed units, was offset by the diminished performance of the 2-bladed turbines. The potential benefits associated with the heterogeneous wind farm for the $S_x = 10$ layout were negligible due to the longer recovery distances resulting in uncoupled behavior of consecutive turbine rows.

Despite that the power performance of the heterogeneous wind farm did not improve over the baseline, it may offer investment advantages. One immediate economic advantage is the lower costs of manufacturing and transportation associated with the 2-bladed rotors. A previous feasibility study reported that for offshore wind farms under certain operating conditions, 2-bladed turbines have lower energy cost than the 3-bladed units [18]. Furthermore, implementing load-reduction techniques like teetering hub to mitigate the effect of load imbalance on the 2-bladed rotor is expected to further improve the power performance of the heterogeneous configuration by reducing the higher inherent fluctuations of the 2-bladed rotors.

Acknowledgments

This work was supported by the Department of Mechanical Science and Engineering, UIUC, as part of the start-up package of L. P. C. Also, T. C. and Y. P. gratefully acknowledge the support of NSF-CBET 1335868 grant, as well as a computing time allocation on Stampede cluster from the TACC super-computing center at Austin, Texas, under the XSEDE grant TG-ENG150019.

References

[1] R. Wiser, E. Lantz, T. Mai, J. Zayas, E. DeMeo, E. Eugeni, J. Lin-Powers, R. Tusing, Wind vision: a new era for wind power in the United States, Electr. J. 28 (9) (2015) 120–132.

[2] M. Rothe, B. Thomsen, A. Zervos, S. Nielsen, J. Bömer, L. Pirazzi, I. Doornbos, I. Cruz, L. Andersson, J. Overton, A Vision for Europe in 2030, Advisory Council of the European Wind Energy Technology Platform, 2006.

[3] Z. Wang, J. Shi, Y. Zhao, Technology Roadmap: China Wind Energy Development Roadmap 2050, International Energy Agency and Energy Research Institute, Paris, France, 2011, p. 56.

[4] M.Z. Jacobson, M.A. Delucchi, Z.A. Bauer, S.C. Goodman, W.E. Chapman, M.A. Cameron, C. Bozonnat, L. Chobadi, H.A. Clonts, P. Enevoldsen, et al., 100% clean and renewable wind, water, and sunlight all-sector energy roadmaps for 139 countries of the world, Joule 1 (1) (2017) 108–121.

[5] G. Mosetti, C. Poloni, B. Diviacco, Optimization of wind turbine positioning in large windfarms by means of a genetic algorithm, J. Wind Eng. Ind. Aerod. 51 (1) (1994) 105–116.

[6] S. Grady, M. Hussaini, M.M. Abdullah, Placement of wind turbines using genetic algorithms, Renew. Energy 30 (2) (2005) 259–270.

[7] J.S. González, A.G.G. Rodriguez, J.C. Mora, J.R. Santos, M.B. Payan, Optimization of wind farm turbines layout using an evolutive algorithm, Renew. Energy 35 (8) (2010) 1671–1681.

[8] J. Feng, W.Z. Shen, Solving the wind farm layout optimization problem using random search algorithm, Renew. Energy 78 (2015) 182–192.

[9] S. Chowdhury, J. Zhang, A. Messac, L. Castillo, Unrestricted wind farm layout optimization (UWFLO): investigating key factors influencing the maximum power generation, Renew. Energy 38 (1) (2012) 16–30.

[10] X. Yang, S. Kang, F. Sotiropoulos, Computational study and modeling of turbine spacing effects in infinite aligned wind farms, Phys. Fluids 24 (11) (2012), 115107.

[11] J. Meyers, C. Meneveau, Optimal turbine spacing in fully developed wind farm boundary layers, Wind Energy 15 (2) (2012) 305–317.

[12] L.P. Chamorro, R. Arndt, F. Sotiropoulos, Turbulent flow properties around a staggered wind farm, Bound-Lay Meteorol. 141 (3) (2011) 349–367.

[13] L.P. Chamorro, N. Tobin, R.E.A. Arndt, F. Sotiropoulos, Variable-sized wind turbines are a possibility for wind farm optimization, Wind Energy 17 (10) (2014) 1483–1494.

[14] T. Chatterjee, Y.T. Peet, Exploring the benefits of vertically staggered wind farms: understanding the power generation mechanisms of turbines operating at different scales, Wind Energy (2018a) 1–19, https://doi.org/10.1002/we.2284.

[15] J. Feng, W.Z. Shen, Design optimization of offshore wind farms with multiple types of wind turbines, Appl. Energy 205 (2017) 1283–1297.

[16] M. Adaramola, P.-Å. Krogstad, Experimental investigation of wake effects on wind turbine performance, Renew. Energy 36 (8) (2011) 2078–2086.

[17] G. Corten, P. Schaak, E. Bot, More power and less loads in wind farms:Heat and flux, in: European Wind Energy Conference & Exhibition, London, UK, 2004.

[18] A.J. Paul, A Comparative Analysis of the Two-Bladed and the Three-Bladed Wind Turbine for Offshore Wind Farms, Master's Thesis, Technical University of Delft, Netherlands, 2010.

[19] T. Bhatti Shikha, D. Kothari, New horizons for offshore wind energy: shifting paradigms and challenges, Energy Sources 27 (4) (2005) 349–360.

[20] P. Jamieson, Innovation in Wind Turbine Design, John Wiley & Sons, 2011.

[21] F. Mühle, M.S. Adaramola, L. Sretran, The effect of the number of blades on wind turbine wake-a comparison between 2-and 3-bladed rotors, in: J Phys Conf Ser, vol. 753, IOP Publishing, 2016, 032017.

[22] D. Medici, Experimental Studies of Wind Turbine Wakes: Power Optimisation and Meandering, Ph.D. thesis, KTH, 2005.

[23] A.J. Newman, R.B. Cal, L. Castillo, Blade number effects in a scaled down wind farm, Renew. Energy 81 (2015) 472–481.

[24] R. Adrian, C. Meinhart, C. Tomkins, Vortex organization in the outer region of the turbulent boundary layer, J. Fluid Mech. 422 (2000) 1–54.

[25] E. Johnson, A.A. Fontaine, M.L. Jonson, R.S. Meyer, W.A. Straka, S. Young, C. van Dam, H. Shiu, M. Barone, A1: 8.7 scale water tunnel test of an axial flow water turbine, in: Proceedings of the 1rst Marine Energy Technology Symposium, METS13, Washington Dc, 2013.

[26] H. Shiu, C. van Dam, E. Johnson, M. Barone, R. Phillips, W. Straka, A. Fontaine, M. Jonson, A design of a hydrofoil family for current-driven marine-hydrokinetic turbines, in: Proceedings of the 20th International Conference on Nuclear Engineering and the American Society of Mechanical Engineers 2012 Power Conference, Anaheim, CA, USA, 30 July–3 August, 2012, pp. 839–847.

[27] N. Tobin, A.M. Hamed, L.P. Chamorro, An experimental study on the effects of winglets on the wake and performance of a model wind turbine, Energies 8 (2015a) 11955–11972.

[28] Y. Jin, H. Liu, R. Aggarwal, A. Singh, L.P. Chamorro, Effects of freestream turbulence in a model wind turbine wake, Energies 9 (10) (2016) 830.

[29] L.P. Chamorro, F. Porté-Agel, A wind-tunnel investigation of wind-turbine wakes: boundary-layer turbulence effects, Bound-Lay Meteorol. 132 (2009) 129–149.

[30] Y. Ohya, Wind-tunnel study of atmospheric stable boundary layers over a rough surface, Bound-Lay Meteorol. 98 (1) (2001) 57–82.

[31] P. Fischer, J. Lottes, D. Pointer, A. Siegel, Petascale algorithms for reactor hydrodynamics, J. Phys. Conf. Ser. 125 (2008), 012076.

[32] M.O. Deville, P.F. Fischer, E.H. Mund, High-Order Methods for Incompressible Fluid Flow, Cambridge University Press, Cambridge, UK, 2002.

[33] P.J. Mason, D.J. Thompson, Stochastic backscatter in large-eddy simulations of boundary layers, J. Fluid Mech. 242 (1992) 51–78.

[34] T. Chatterjee, Y.T. Peet, Effect of artificial length scales in large eddy simulation of a neutral atmospheric boundary layer flow: a simple solution to log-layer mismatch, Phys. Fluids 29 (2017), 075175.

[35] E. Bou-Zeid, C. Meneveau, M. Parlange, A scale-dependant Lagrangian dynamic model for large eddy simulation of complex turbulent flows, Phys. Fluids 415 (2005), 025125.

[36] N. Troldborg, Actuator Line Modeling of Wind Turbine Wakes, Ph.D. thesis, Technical University of Denmark, 2008.

[37] Tjæreborg Wind Turbine (Esbjerg): Geometric and Operational Data, Department of Fluid Mechanics, 1990. DTH, DK 2800, Lyngby VK-184.

[38] M.J. Churchfield, S. Lee, P.J. Moriarty, L.A. Martinez, S. Leonardi, G. Vijayakumar, J.G. Brasseur, A Large-Eddy Simulation of Wind-Plant Aerodynamics, 2012. AIAA Paper 2012-0537.

[39] M. Calaf, C. Meneveau, J. Meyers, Large eddy simulation study of fully developed wind-turbine array boundary layers, Phys. Fluids 22 (2010), 015110.

[40] C. VerHulst, C. Meneveau, Large eddy simulation study of the kinetic energy entrainment by energetic turbulent flow structures in large wind farms, Phys. Fluids 8 (2014), 025113.

[41] T. Chatterjee, Y. Peet, Actuator Line Wind Turbine Simulations in Atmospheric Turbulent Flows Using Spectral Element Method, Kissimmmee, Florida, 2015. AIAA paper 2015–0727, 5 - 9 January 2015.

[42] T. Chatterjee, Y. Peet, Large Eddy Simulation of a 3 × 3 Wind Turbine Array Using Actuator Line Model with Spectral Elements, 2016. AIAA paper 2016–1988, 04 - 8 January 2016, San Diego, California.

[43] T. Chatterjee, N.W. Cherukuru, Y. Peet, R. Calhoun, Incorporating Realistic Geophysical Effects of Mean Wind from LIDAR Measurements in Large Eddy Simulation of Wind Turbine Arrays, Grape Vine, Texas, 2016. AIAA paper 2017–1165, 09- 13 January 2017.

[44] S. Dong, G. Karniadakis, C. Chryssostomidis, A robust and accurate outflow boundary condition for incompressible flow simulations on severely- truncated unbounded domains, J. Comput. Phys. 261 (2014) 83–105.

[45] T. Chatterjee, Y.T. Peet, Contribution of large scale coherence to wind turbine power: a large eddy simulation study in periodic wind farms, Phys. Rev. Fluids 3 (2018b), 034601.

[46] J. Jiménez, P. Moin, The minimal flow unit in near-wall turbulence, J. Fluid Mech. 225 (1991) 221–240.

[47] J. Jiménez, J.D. Álamo, O. Flores, The large-scale dynamics of near-wall turbulence, J. Fluid Mech. 505 (2004) 179–199.

[48] A. Loranzo-Durán, J. Jiménez, Effect of the computational domain on direct simulations of turbulent channels up to $Re_\tau = 4200$, Phys. Fluids 26 (2014), 011702.

[49] N. Hamilton, H.S. Kang, C. Meneveau, R.B. Cal, Statistical analysis of kinetic energy entrainment in a model wind turbine array boundary layer, J. Renew. Sustain. Energy 4 (2012), 063105.

[50] L.P. Chamorro, S.J. Lee, D. Olsen, C. Milliren, J. Marr, R. Arndt, F. Sotiropoulos, Turbulence effects on a full–scale 2.5 MW horizontal–axis wind turbine under neutrally stratified conditions, Wind Energy 18 (2) (2015) 339–349.

[51] K.L. Wu, F. Porte-Agel, Flow adjustment inside and around large finite-size wind farms, Energies 10 (12) (2017) 2164.

[52] J. Bleeg, M. Purcell, R. Ruisi, E. TRaiger, Wind farm blockage and the consequences of neglecting its impact on energy production, Energies 11 (6) (2018) 1609.

[53] L.P. Chamorro, F. Porté-Agel, Turbulent flow inside and above a wind farm: a wind-tunnel study, Energies 4 (2011) 1916–1936.

[54] Y.T. Peet, T. Chatterjee, The contribution of large scale structures in the power generation of finite scale wind farms using large eddy simulation, in: TSFP10, 10th International Symposium on Turbulence and Shear Flow Phenomena (TSFP10), Chicago, USA, July, 2017, 2017.

[55] L.P. Chamorro, M. Guala, R.E.A. Arndt, F. Sotiropoulos, On the evolution of turbulent scales in the wake of a wind turbine model, J. Turbul. 13 (2012) N27.

[56] V.L. Okulov, I.V. Naumov, R.F. Mikkelsen, I.K. Kabardin, J.N. Sørensen, A regular Strouhal number for large-scale instability in the far wake of a rotor, J. Fluid Mech. 747 (2014) 369–380.

[57] D. Medici, P.H. Alfredsson, Wind turbine near wakes and comparisons to the wake behind a disc, in: 43rd AIAA Aerospace Sciences Meeting and Exhibit-Meeting Papers, 2005, pp. 15593–15604.

[58] H. Liu, Y. Jin, N. Tobin, L.P. Chamorro, Towards uncovering the structure of power fluctuations of wind farms, Phys. Rev. E 96 (2017), 063117.

[59] N. Tobin, H. Zhu, L.P. Chamorro, Spectral behaviour of the turbulence-driven power fluctuations of wind turbines, J. Turbul. 16 (9) (2015b) 832–846.